Joule

CellPress
OPEN ACCESS

Article

Deflecting lithium dendritic cracks in multi-layered solid electrolytes

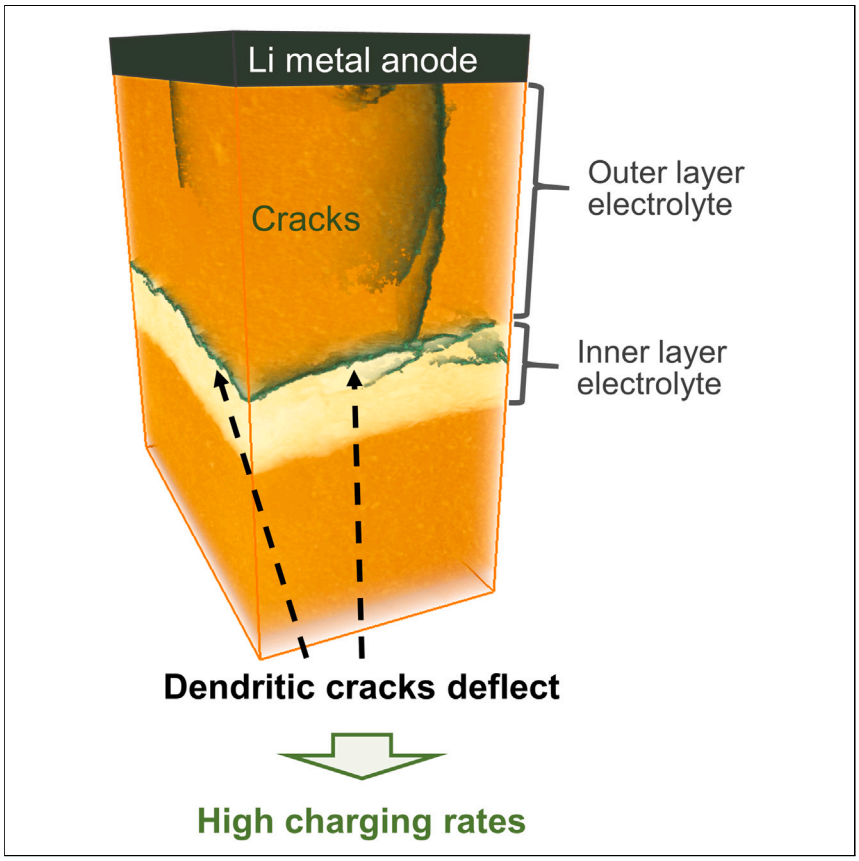

To enhance the charging rate of solid-state batteries with lithium metal anodes and ceramic electrolytes, it is crucial to inhibit lithium dendrite penetration within the solid electrolytes. In this study, we demonstrate that dendrite growth can be effectively impeded by deflecting dendritic cracks along weak interfaces within multi-layered solid electrolytes.

Bingkun Hu, Shengming Zhang, Ziyang Ning, ..., Genoveva Burca, T. James Marrow, Peter G. Bruce

james.marrow@materials.ox.ac.uk (T.J.M.)
peter.bruce@materials.ox.ac.uk (P.G.B.)

Highlights

Dendrite growth is inhibited by crack deflection in multi-layered solid electrolytes

Dendrite crack deflects at interfaces between layers with dissimilar elastic moduli

Crack deflects in the inner layer, adopting a preferred orientation of dense particles

Hu et al., Joule *8*, 1–16
September 18, 2024
Published by Elsevier Inc.
https://doi.org/10.1016/j.joule.2024.06.024

Please cite this article in press as: Hu et al., Deflecting lithium dendritic cracks in multi-layered solid electrolytes, Joule (2024), https://doi.org/10.1016/j.joule.2024.06.024

Joule

CellPress
OPEN ACCESS

Article

Deflecting lithium dendritic cracks in multi-layered solid electrolytes

Bingkun Hu,[1] Shengming Zhang,[1] Ziyang Ning,[1,2] Dominic Spencer-Jolly,[1,3] Dominic L.R. Melvin,[1] Xiangwen Gao,[1,4] Johann Perera,[1] Shengda D. Pu,[1] Gregory J. Rees,[1] Longlong Wang,[1] Lechen Yang,[1] Hui Gao,[1] Shashidhara Marathe,[5] Genoveva Burca,[5,6,7] T. James Marrow,[1,*] and Peter G. Bruce[1,8,9,*]

SUMMARY

Charging current densities of solid-state batteries with lithium metal anodes and ceramic electrolytes are severely limited due to lithium dendrites that penetrate the electrolyte leading to a short circuit. We show that dendrite growth can be inhibited by different crack deflection mechanisms when multi-layered solid electrolytes, such as $Li_6PS_5Cl/Li_3ScCl_6/Li_6PS_5Cl$ and $Li_6PS_5Cl/Li_{10}GeP_2S_{12}/Li_6PS_5Cl$, are employed but not when the inner layer is Li_3PS_4. X-ray tomographic imaging shows crack deflection along mechanically weak interfaces between solid electrolytes as a result of local mismatches in elastic moduli. Cracks are also deflected laterally within Li_3ScCl_6, which contains preferentially oriented particles. Deflection occurs without lithium being present. In cases where the inner layers react with lithium, the resulting decomposition products can fill and block crack propagation. All three mechanisms are effective at low stack pressures. Operating at 2.5 MPa, multi-layered solid electrolytes $Li_6PS_5Cl/Li_3ScCl_6/Li_6PS_5Cl$ and $Li_6PS_5Cl/Li_{10}GeP_2S_{12}/Li_6PS_5Cl$ can achieve lithium plating at current densities exceeding 15 mA cm^{-2}.

CONTEXT & SCALE

Lithium metal solid-state batteries with ceramic electrolytes promise to surpass the energy density limits and address the safety issues of commercial lithium-ion batteries with liquid electrolytes. However, their charging rate is constrained by lithium filament (dendrite) penetration within the solid electrolyte at practical charging currents. In this work, we demonstrate that even if dendrite initiation cannot be avoided, propagation across the electrolyte can be inhibited within multi-layered solid electrolytes through dendritic crack deflection along the interfaces between layers with dissimilar elastic moduli, or within the inner layer exhibiting a preferred orientation of particles.

INTRODUCTION

A range of strategies have been explored to inhibit the growth of lithium dendrite cracks on charging solid-state batteries composed of a lithium anode and ceramic electrolyte.[1–5] Lithium dendrites formed at practical charging currents penetrate the solid electrolyte, leading eventually to short-circuit and cell failure.[6–14] As a result, their mitigation is one of the major challenges in the field. Approaches including modification of the solid electrolyte surface in contact with the lithium metal anode,[15,16] the interposing of layers between the solid electrolyte and lithium anode,[4,17,18] and modifying the microstructure of the solid electrolyte[19,20] have all been considered. Recently, introducing a different solid electrolyte as an inner layer sandwiched between two layers of the primary solid electrolyte to form a multi-layer structure has been reported to inhibit dendrite crack propagation by a mechanism involving chemical reaction between the lithium metal dendrite and the inner layer material that blocks the crack through the expansion screw effect.[21]

Here, we examine the role of solid electrolyte inner layers in cells where these solid electrolytes are placed between two outer layers of the solid electrolyte, Li_6PS_5Cl, argyrodite. Specifically, we focus on Li_3ScCl_6 and $Li_{10}GeP_2S_{12}$ inner layers as archetypal examples of a halide and sulfide solid electrolyte, respectively, with high ionic conductivities. Additionally, we include a Li_3PS_4 inner layer in the investigation, as it has a similar elastic modulus to Li_6PS_5Cl, with the aim of shedding light on the

Please cite this article in press as: Hu et al., Deflecting lithium dendritic cracks in multi-layered solid electrolytes, Joule (2024), https://doi.org/10.1016/j.joule.2024.06.024

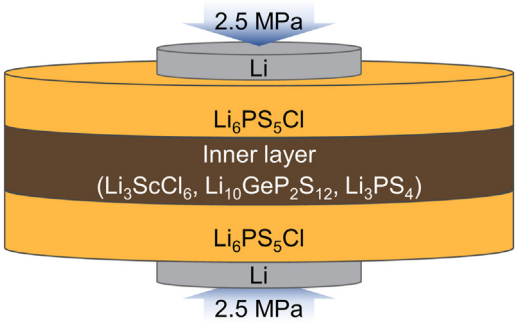

Figure 1. Schematic of solid-state cell with multi-layered solid electrolyte architecture

An inner layer of Li_3ScCl_6, $Li_{10}GeP_2S_{12}$, or Li_3PS_4 is sandwiched between an outer layer of Li_6PS_5Cl. Li metal electrodes are attached onto both sides of the layered electrolyte. All cells are operated at a stack pressure of 2.5 MPa.

underlying mechanisms. We show that when lithium dendrite cracks reach the inner layers of Li_3ScCl_6 and $Li_{10}GeP_2S_{12}$, they are deflected along the interface between them and the Li_6PS_5Cl layer. The mechanism does not involve reactivity with lithium, in contrast to the previous study of $Li_{10}GeP_2S_{12}$ and $Li_{9.54}Si_{1.74}(P_{0.9}Sb_{0.1})_{1.44}$ as the inner layer with $Li_{5.5}PS_{4.5}Cl_{1.5}$ as the outer layers, where the deflected cracks are dry (contain no lithium).[21] This is in accord with the recent observations that lithium dendrites penetrate the ceramic electrolyte by dry cracking, with Li at the back of the crack driving the crack tip forward by wedge opening.[22,23] The crack deflection occurs for inner layers for which the Young's modulus is significantly different from that of the outer solid electrolyte, leading to a mechanically weak interface. Deflection along the interface occurs whether or not there is a chemical reaction between the outer and inner layer solid electrolyte materials at the interface (Li_6PS_5Cl reacts with Li_3ScCl_6 but not with $Li_{10}GeP_2S_{12}$). A minority of the dendritic cracks can pass into the inner layer. In the case of Li_3ScCl_6, which has a plate-like particle morphology, the inner layer microstructure exhibits strong preferred orientation of the dense particles, with the long axes of the particles parallel to the interfaces between the layers, and as a result, the cracks within the inner layer exhibit significant lateral deflection. Therefore, Li_3ScCl_6 introduces two processes by which dendritic cracks can be deflected. In the case of $Li_{10}GeP_2S_{12}$, the microstructure is similar in all directions and the crack passes more directly across the inner layer. When lithium metal is present in the dendritic crack within the $Li_{10}GeP_2S_{12}$ inner layer, reaction between them fills the cracks, likely by decomposition products that have a higher molar volume than $Li_{10}GeP_2S_{12}$,[21,24] in agreement with the expansion screw effect proposed by Ye and Li.[21] Both crack deflection and crack filling enhance the resistance of the layered electrolytes to transverse cracking and dendrite penetration. In all cases when the inner layer is present, it is possible to plate lithium at currents over 15 mA cm^{-2} without short-circuit, whereas the same cell under the same conditions shorts at 2.75 mA cm^{-2} when the electrolyte is Li_6PS_5Cl alone.

RESULTS AND DISCUSSION

Solid-state cells were constructed with Li_6PS_5Cl as the outer electrolyte layers and with lithium metal electrodes. The solid electrolytes Li_3ScCl_6, $Li_{10}GeP_2S_{12}$, and Li_3PS_4 were incorporated as inner layers within the solid electrolyte. The cell structure is shown schematically in Figure 1. Electrolyte and cell formation are described in the experimental procedures. All cells were operated at a low stack pressure of 2.5 MPa, representative of pressures possible in practical cells.

Li_3ScCl_6

The voltage profile of the cell Li/Li_6PS_5Cl/Li_3ScCl_6/Li_6PS_5Cl/Li during cycling as a function of stepwise increases in current density is shown in Figure 2A. The cell

[1]Department of Materials, University of Oxford, Oxford OX1 3PH, UK

[2]Fujian Science & Technology Innovation Laboratory for Energy Devices (21C Lab), Ningde 352100, China

[3]School of Metallurgy and Materials, University of Birmingham, Birmingham B15 2SE, UK

[4]Future Battery Research Center, Global Institute of Future Technology, Shanghai Jiao Tong University, Shanghai 200240, China

[5]Diamond Light Source, Harwell Campus, Didcot OX11 0DE, UK

[6]STFC-Rutherford Appleton Laboratory, ISIS Facility, Harwell OX11 0QX, UK

[7]Faculty of Science and Engineering, The University of Manchester, Manchester M13 9PL, UK

[8]Department of Chemistry, University of Oxford, Oxford OX1 3QZ, UK

[9]Lead contact

*Correspondence: james.marrow@materials.ox.ac.uk (T.J.M.), peter.bruce@materials.ox.ac.uk (P.G.B.)

https://doi.org/10.1016/j.joule.2024.06.024

Please cite this article in press as: Hu et al., Deflecting lithium dendritic cracks in multi-layered solid electrolytes, Joule (2024), https://doi.org/10.1016/j.joule.2024.06.024

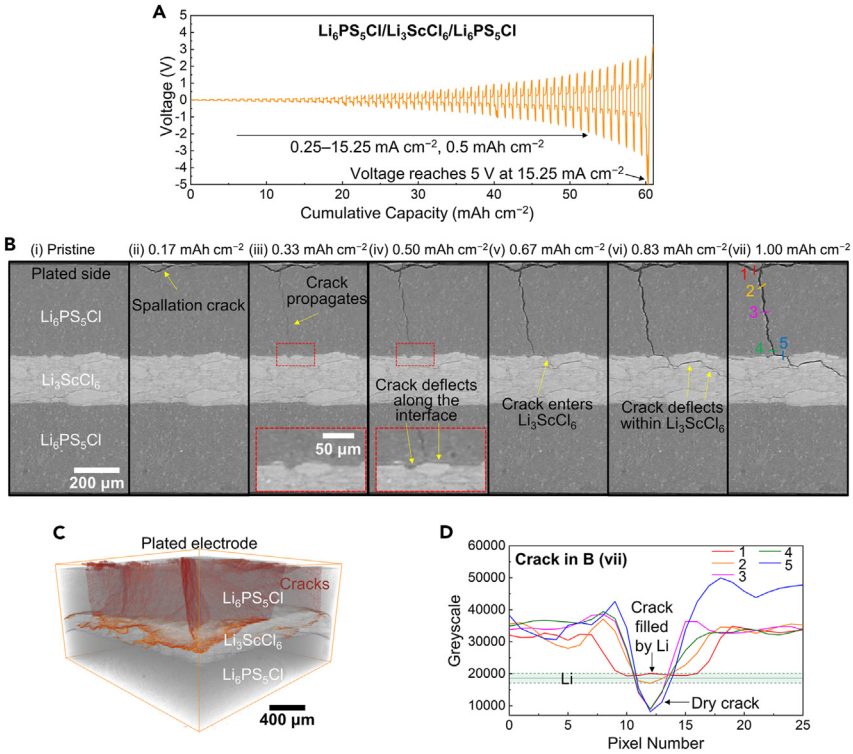

Figure 2. Electrochemical data and XCT virtual cross-sections from the Li/Li_6PS_5Cl/Li_3ScCl_6/Li_6PS_5Cl/Li cell

(A) The voltage profile on cell cycled with stepwise increasing current density from 0.25 to 15.25 mA cm^{-2} under 2.5 MPa. The current step is 0.25 mA cm^{-2} and the plating/stripping capacity is 0.5 mAh cm^{-2} per half cycle.

(B) XCT before plating (i), and after plating 0.17 (ii), 0.33 (iii), 0.50 (iv), 0.67 (v), 0.83 (vi), 1.00 mAh cm^{-2} (vii), indicating that the crack deflection initiates at the Li_6PS_5Cl/Li_3ScCl_6 interface and propagates laterally both along the interface and within the Li_3ScCl_6 inner layer. The electrodes were removed from the images for clarity. Insets in (iii) and (iv) are magnified images of the regions indicated by red boxes.

(C) 3D rendered cracks within the cell at stage (vii).

(D) Grayscale profiles across the crack at different positions along the crack indicated by lines 1–5 in (Bvii).

can survive a current density of at least 15.25 mA cm^{-2} without short-circuit, compared with 2.75 mA cm^{-2} for Li_6PS_5Cl alone under the same conditions, (Figure S1) demonstrating the effectiveness of introducing such an inner layer (Figure 2A). As shown previously, polarization of such symmetric cells arises from voiding at the interfaces on stripping.[8] X-ray computed tomography (XCT) collected as a function of the charge passed is also shown in Figure 2B. The experimental set-up is described in the experimental procedures. The virtual cross-sections from the XCT data while plating lithium at the top electrode show the typical spalling of the lithium dendritic cracks back to the interface between the lithium metal and the solid electrolyte, as well as the progression of the transverse crack across the Li_6PS_5Cl toward the interface with the Li_3ScCl_6. When the transverse crack reaches the Li_3ScCl_6, it is deflected along the interface (Figures 2Biii and 2Biv) rather than continuing unabated toward the other electrode (bottom). After progressing along the interface, it then enters the inner layer, (Figure 2Bv) where the crack is further deflected laterally within the inner layer (Figures 2Bvi and 2Bvii). The 3D rendered XCT image in Figure 2C is consistent with the cross-sections showing crack propagation

Please cite this article in press as: Hu et al., Deflecting lithium dendritic cracks in multi-layered solid electrolytes, Joule (2024), https://doi.org/10.1016/j.joule.2024.06.024

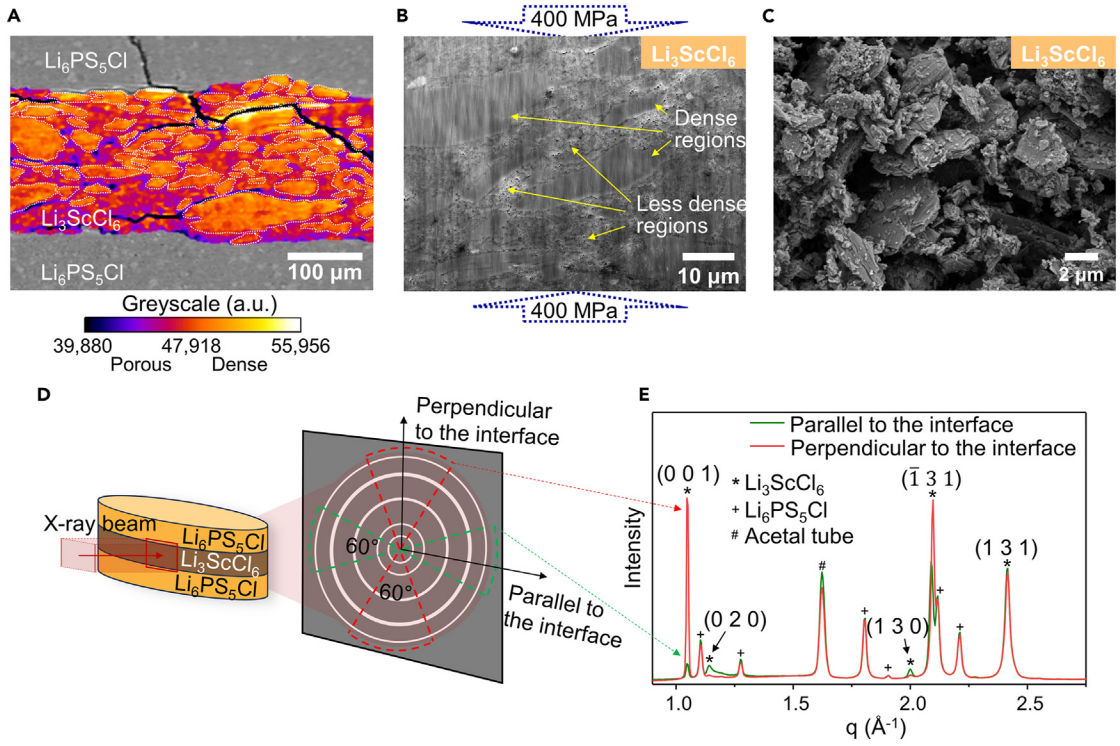

Figure 3. Characterization of the Li_3ScCl_6 microstructure

(A) Magnified XCT image extracted from Figure 2Bvii. The color map is based on the gray scale attenuation from the X-ray data and is used to make the microstructural inhomogeneity clear. More attenuating (denser) regions (shown in orange and highlighted by white dotted boundary lines) separated by less dense (shown in red) regions. The comparison with the original image can be found in Figure S4.

(B) PFIB-SEM image shows dense regions surrounded by less dense regions in Li_3ScCl_6. The direction of the uniaxial pressure applied during electrolyte fabrication is indicated by blue arrows.

(C) SEM image of the pristine Li_3ScCl_6 powder.

(D) Schematic illustrating orientation of incident X-ray beam impinging on the $Li_6PS_5Cl/Li_3ScCl_6/Li_6PS_5Cl$ cell. Diffraction rings with highlighting of the azimuthal zones (bounded by dotted lines) with an azimuthal range of $\pm 30°$ around the axes parallel and perpendicular to the interfaces between Li_6PS_5Cl and Li_3ScCl_6 are integrated into 1D plots, respectively.

(E) Integrated diffraction rings within the azimuthal ranges shown in (D), lead to the parallel and perpendicular 1D diffraction patterns.

along the interface and within the inner layer, the latter exhibiting significant lateral deflection. This is in contrast to the monolithic Li_6PS_5Cl, in which a transverse crack penetrates through the whole electrolyte without deflection (Figure S2). Grayscale analysis of various locations along the crack in Figure 2Bvii is presented in Figure 2D. This shows crack deflection along the interface and into the inner layer occurs without the presence of lithium metal in the crack. Therefore, the crack inhibition by deflection observed here occurs mechanically, and this does not result from the reaction between the Li dendrite and the inner layer. The mechanism is different from that reported previously by Ye and Li.[21] In the previous study, the authors considered lithium metal to be reacting with the $Li_{10}GeP_2S_{12}$ or $Li_{9.54}Si_{1.74}(P_{0.9}Sb_{0.1})_{1.44}$ inner layer forming products that block the crack by an expansion screw mechanism. What, then, are the origins of these crack deflections at the interface between different solid electrolytes and within the inner layer, when not due to reaction with lithium?

The microstructure of the Li_3ScCl_6 inner layer is presented in Figure 3. The XCT virtual cross-section (Figure 3A) shows its heterogeneous nature, with more attenuating (denser) regions (shown in orange and highlighted by white dotted boundary lines) separated by less dense (shown in red) regions. The coloration is based on a

Please cite this article in press as: Hu et al., Deflecting lithium dendritic cracks in multi-layered solid electrolytes, Joule (2024), https://doi.org/10.1016/j.joule.2024.06.024

gray scale analysis of the X-ray attenuation and is used here to make the contrast clearer. The heterogeneous nature of the microstructure, with dense particles separated by porous regions, is also apparent in the plasma focused ion beam scanning electron microscopy (PFIB-SEM) cross-section in Figure 3B. An SEM image of the pristine Li_3ScCl_6 powder is shown in Figure 3C. It consists of relatively large particles with a plate-like morphology of high aspect ratio separated by many smaller particles. In forming the multi-layer solid electrolyte, a pressure of 400 MPa was applied, resulting in the microstructure in Figure 3B. The pristine powders, especially the large particles with a high aspect ratio(Figure 3C) consolidate to form the dense particles in Figure 3B (the dense regions in Figure 3B are greater in size than the largest particles seen in the pristine powder in Figure 3C), while the smaller particles of the pristine material make up the more porous regions in Figure 3B. The large dense particles are preferentially oriented with their long axes parallel to the interfaces between the Li_3ScCl_6 and Li_6PS_5Cl. In other words, the application of pressure to the powder with high aspect ratio particles has resulted in a stratified microstructure(Figure 3B). This is distinct from Li_6PS_5Cl, which exhibits an isotropic microstructure (Figure S3). After releasing the pressure, the Li_3ScCl_6 inner layer will expand, inducing internal tensile stresses. For a stiff inclusion (dense particle in our case), the expansion of the inner layer will create higher tensile stress at the inclusion/matrix (lower stiffness porous regions) boundaries, especially at the corners of the inclusion.[25,26] The stress concentration tends to fracture the boundaries and leads to low boundary strength. Indeed, some weakly bonded boundaries can be observed surrounding these dense regions in the pristine state (Figure 2Bi). These weak boundaries may then act as the path of least resistance for propagating cracks.[27,28] When the transverse crack in the Li_6PS_5Cl solid electrolyte reaches the interface with the Li_3ScCl_6 (Figure 2Biv), it encounters a dense Li_3ScCl_6 particle that encourages propagation along the interface but also around the particle entering the inner layer within the lower density regions of the microstructure (Figure 2Bv). The preferred orientation of the dense particles within the Li_3ScCl_6 inner layer encourages propagation of the dendritic crack in the predominantly lateral direction (Figures 2Bvii and 3A), providing a mechanism for the crack deflection process within the inner layer. Powder X-ray diffraction (PXRD) data were extracted from the synchrotron X-ray beam entering the Li_3ScCl_6 inner layer parallel to the interfaces between the two solid electrolytes, as shown in Figure 3D. Integrating the diffraction rings only within the angular range $\pm 30^\circ$ around the axes parallel and perpendicular to the interfaces between Li_6PS_5Cl and Li_3ScCl_6 (Figure 3D) leads to the two PXRD patterns shown in Figure 3E. Li_3ScCl_6 adopts a layered crystal structure. The intensities of the Li_3ScCl_6 peaks with *hkl* values corresponding to reflections predominantly along the *c*-direction, i.e., perpendicular to the layers, show very significant differences between the parallel and perpendicular powder patterns, indicating that the crystallites exhibit a high degree of preferred orientation with the long axes of the crystallites aligned parallel to the interfaces. There is little difference in the intensities of the powder diffraction patterns for the Li_6PS_5Cl phase within which the cells were located for the diffraction measurements, in accord with Li_6PS_5Cl not possessing a highly anisotropic crystal structure.[29] The PXRD data considers only the orientation and length scales corresponding to the crystallographically coherent regions of the crystal structure, whereas the SEM and XCT probe much larger dimensions. However overall all these techniques indicate the strongly stratified nature of the preferred orientation of the Li_3ScCl_6 inner layer.

$Li_{10}GeP_2S_{12}$

Figure 4A shows XCT virtual cross-sections from the cell, Li/Li_6PS_5Cl/$Li_{10}GeP_2S_{12}$/Li_6PS_5Cl/Li, i.e., where the Li_3ScCl_6 inner layer has been replaced by $Li_{10}GeP_2S_{12}$.

Please cite this article in press as: Hu et al., Deflecting lithium dendritic cracks in multi-layered solid electrolytes, Joule (2024), https://doi.org/10.1016/j.joule.2024.06.024

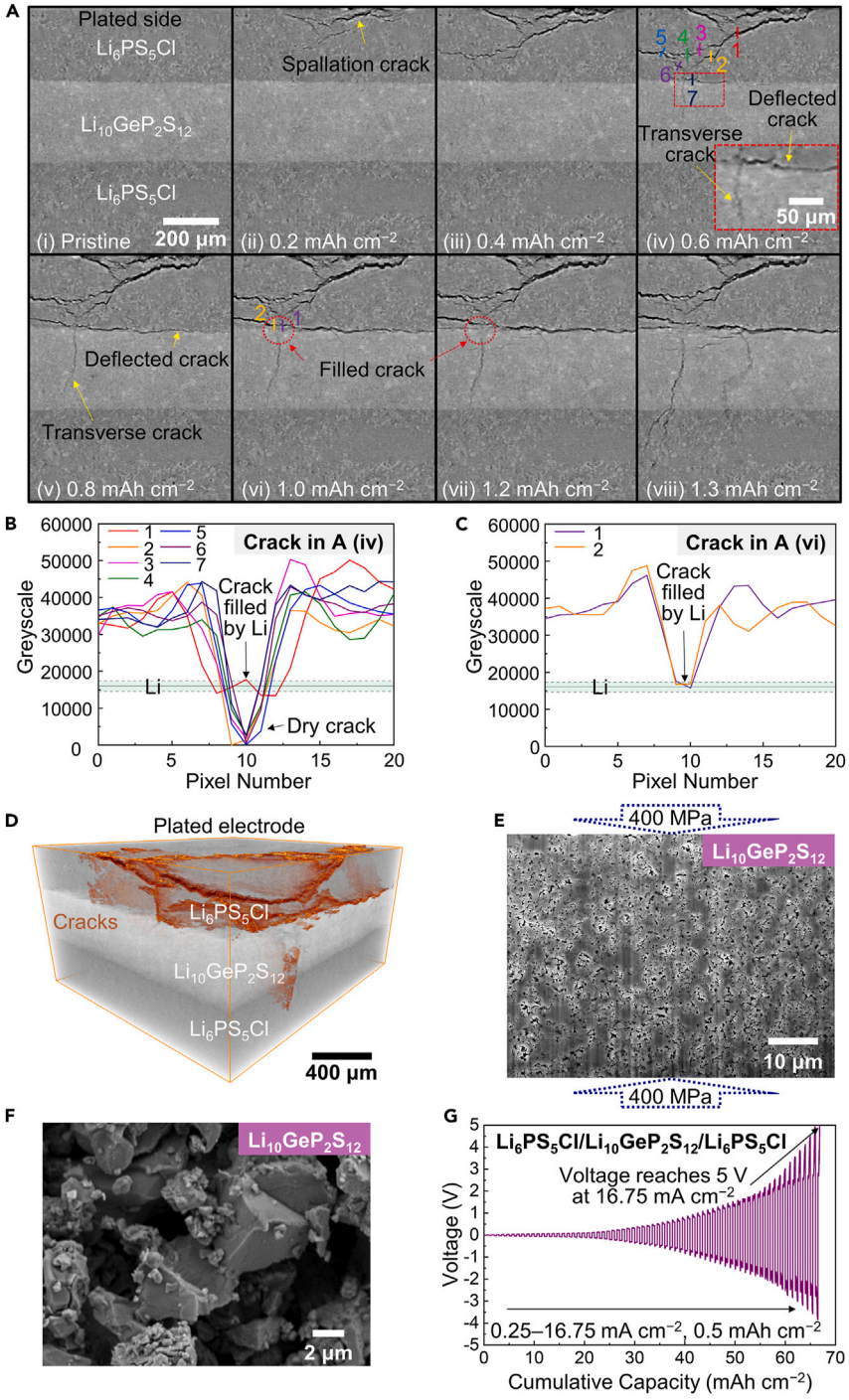

Figure 4. XCT virtual cross-sections, SEM images, and electrochemical data from the Li/Li_6PS_5Cl/$Li_{10}GeP_2S_{12}$/Li_6PS_5Cl/Li cell

(A) XCT before plating (i), and after plating 0.2 (ii), 0.4 (iii), 0.6 (iv), 0.8 (v), 1.0 (vi), 1.2 (vii), 1.3 mAh cm^{-2} (viii) showing crack deflection along the Li_6PS_5Cl/$Li_{10}GeP_2S_{12}$ interface and transverse crack propagation. The electrodes were removed from the images for clarity.

(B) Grayscale profiles across the crack at different positions along the crack indicated by 1–7 in (Aiv).

(C) Grayscale profiles along the crack from two positions at the Li_6PS_5Cl/$Li_{10}GeP_2S_{12}$ interface indicated by 1 and 2 in (Avi).

(D) 3D rendered cracks within the electrolyte in (Aviii).

Please cite this article in press as: Hu et al., Deflecting lithium dendritic cracks in multi-layered solid electrolytes, Joule (2024), https://doi.org/10.1016/j.joule.2024.06.024

Figure 4. *Continued*

(E) PFIB-SEM image shows an isotropic microstructure for $Li_{10}GeP_2S_{12}$. The uniaxial pressure applied to the electrolyte during fabrication is indicated by blue arrows.

(F) SEM image of the pristine $Li_{10}GeP_2S_{12}$ powders.

(G) The voltage profile of a Li/Li_6PS_5Cl/$Li_{10}GeP_2S_{12}$/Li_6PS_5Cl/Li cell cycled at stepwise increasing current density from 0.25 to 16.75 mA cm^{-2} under 2.5 MPa. The current step is 0.25 mA cm^{-2} and the plating/stripping capacity is 0.5 mAh cm^{-2} per half cycle.

The images show that on charging, spallations and transverse cracks form in the Li_6PS_5Cl electrolyte. As observed before for Li_3ScCl_6, when the transverse crack reaches the interface with the inner layer, it deflects significantly along the interface as well as entering the inner layer (Figure 4Aiv onward). Grayscale analysis from different locations along the crack in Figure 4Aiv is shown in Figure 4B. The crack deflecting at the interface and the crack entering the inner layer do so as dry cracks, i.e., without lithium being present in these regions. The 3D rendered image in Figure 4D also shows significant crack deflection along the interface as well as cracks passing through the inner layer relatively unimpeded and into the lower Li_6PS_5Cl solid electrolyte.

Although deflection at the interface between the Li_6PS_5Cl solid electrolyte and the $Li_{10}GeP_2S_{12}$ inner layer is similar to the observations in the case of the Li_3ScCl_6 inner layer, the progression of the dendritic crack through the inner layer is different. The PFIB-SEM of the $Li_{10}GeP_2S_{12}$ inner layer (Figure 4E) shows that the microstructure is isotropic, with no evidence of stratification, unlike the case of Li_3ScCl_6. The pristine $Li_{10}GeP_2S_{12}$ powders consist of isotropic particles, see Figure 4F. Accordingly, the microstructure of the pressed $Li_{10}GeP_2S_{12}$ is not composed of dense regions separated by areas of lower density, with no evidence of particle alignment that would lead to lateral deflection. The isotropic and homogeneous microstructure is in accord with a relatively direct trajectory of the dendritic crack across the inner layer.

With more charge passed, lithium grows down the dry crack to reach the $Li_{10}GeP_2S_{12}$ inner layer, (Figure 4Avi) evidenced by the grayscale analysis of the crack content at locations 1 and 2 in Figure 4Avi and shown in Figure 4C. Examination of the virtual cross-sections in Figures 4Avi and 4Avii shows that in the region of the crack within the inner layer close to the upper interface with Li_6PS_5Cl, the crack appears to be filled, region highlighted by red dashed circles. To investigate this further, a virtual section was taken from the XCT data within the inner layer parallel and close to the upper interface between Li_6PS_5Cl and $Li_{10}GeP_2S_{12}$. The blue lines in the 3D reconstruction of the cell in Figure 5A show the plane on which the virtual sections were taken. The evolution of the structure at this plane with increasing charge passed is shown in the series of images in Figure 5B. The cracks are propagating perpendicular to the plane. The cracks passing through the plane become evident in Figure 5Biii and grow with increasing charge passed, as seen in Figure 5Biv. On passing further charge, in Figure 5Bv, the attenuation contrast is reduced in the regions of the cracks highlighted by the red arrows. The process continues and becomes prevalent in other regions of the cracks with increasing charge passed, e.g., red arrows in Figure 5Bvi. The homogenization of the attenuation is consistent with the cracks being filled with materials of broadly similar scattering to the solid electrolyte, i.e., not or not only Li metal. It is known that Li metal reacts with $Li_{10}GeP_2S_{12}$.[30] We interpret these observations as lithium metal, having now reached the regions of the dry crack just within the inner layer, reacts with the $Li_{10}GeP_2S_{12}$, forming reaction products that fill the cracks. Maximum normal 3D strain maps were constructed from XCT images based on the gradients of local displacements of the ceramic obtained by

Please cite this article in press as: Hu et al., Deflecting lithium dendritic cracks in multi-layered solid electrolytes, Joule (2024), https://doi.org/10.1016/j.joule.2024.06.024

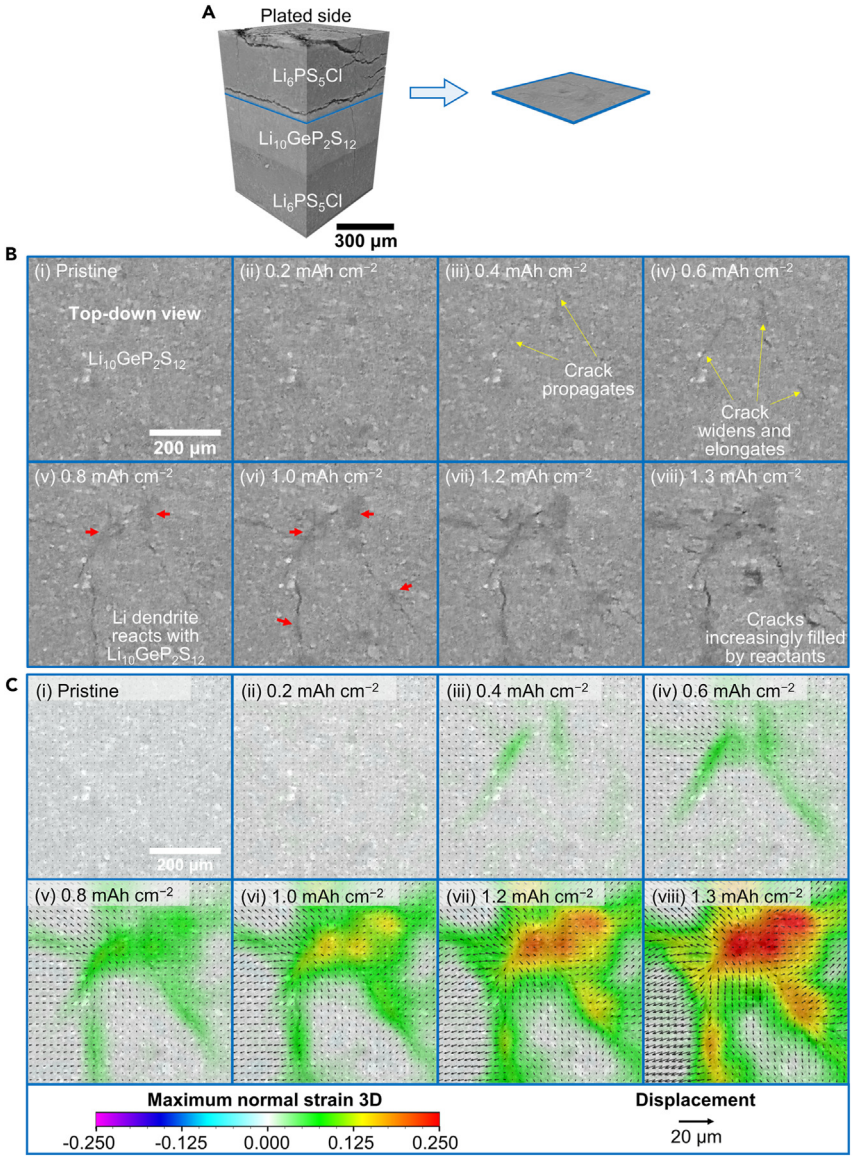

Figure 5. XCT virtual top-down view of the $Li_{10}GeP_2S_{12}$ layer, and the corresponding maximum normal 3D strain map and displacement from DVC analysis

(A) A 3D reconstruction showing the location of the virtual section (blue lines).

(B) XCT virtual top-down view before plating (i), and after plating 0.2 (ii), 0.4 (iii), 0.6 (iv), 0.8 (v), 1.0 (vi), 1.2 (vii), 1.3 mAh cm^{-2} (viii) showing crack formation, growth (yellow arrows), then filling (red arrows), from the reaction between Li and $Li_{10}GeP_2S_{12}$.

(C) The corresponding maps of maximum normal 3D strain (color map) and displacement (arrows, relative to average displacement) of the same region in (B), obtained from DVC analysis of the XCT scans.

digital volume correlation (DVC) analysis.[31] These are reported in Figure 5C for the same virtual sections as in Figure 5B. The strain due to opening of the cracks that pass through the plane on which the section was taken is evident in Figures 5Ciii and 5Civ. As the cracks develop and the lithium reacts with the surrounding $Li_{10}GeP_2S_{12}$ the strain increases, as shown by the orange and red regions in Figures 5Cvii and 5Cviii. The increased tensile strain is in accord with the volume expansion of $Li_{10}GeP_2S_{12}$ resulting from the reaction with the Li.

Please cite this article in press as: Hu et al., Deflecting lithium dendritic cracks in multi-layered solid electrolytes, Joule (2024), https://doi.org/10.1016/j.joule.2024.06.024

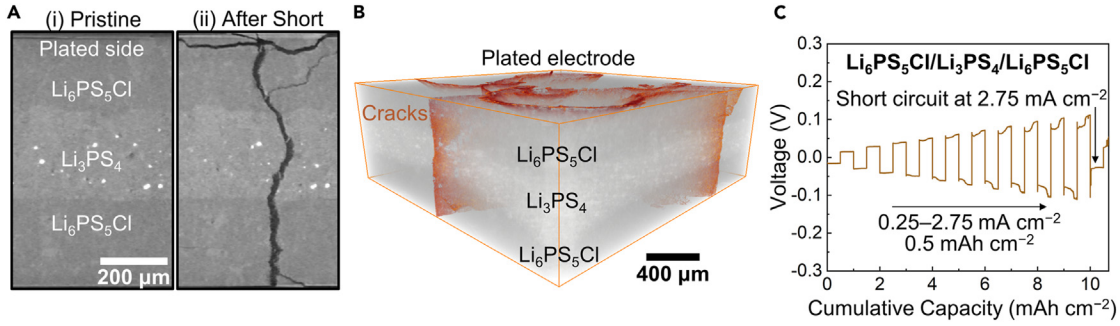

Figure 6. XCT virtual cross-sections and electrochemical data from the Li/Li_6PS_5Cl/Li_3PS_4/Li_6PS_5Cl/Li cell

(A) XCT before plating (i) and after plating until short-circuit (ii) showing a crack propagating through the whole electrolyte without deflection.

(B) 3D rendered cracks within the electrolyte in (Aii).

(C) The voltage profile of a cell cycled at stepwise increasing current density from 0.25 to 2.75 mA cm^{-2} under 2.5 MPa. The current step is 0.25 mA cm^{-2} and the plating/stripping capacity is 0.5 mAh cm^{-2} per half cycle.

The symmetric cell, Li/Li_6PS_5Cl/$Li_{10}GeP_2S_{12}$/Li_6PS_5Cl/Li, can be plated at a current density of at least 16.75 mA cm^{-2} without short-circuit (Figure 4G) compared with 2.75 mA cm^{-2} for Li_6PS_5Cl alone, (Figure S1) demonstrating that crack deflection at the interface as well as filling of the cracks inhibits lithium dendrite propagation. Li_3ScCl_6 is also known to react with Li metal[32,33]; however, we do not see evidence of this reaction occurring in the XCT images for the Li_3ScCl_6 inner layer in Figure 2. Given there is no lithium present in the region of the crack within the inner layer even after passage of 1 mAh cm^{-2} in the case of Li_3ScCl_6, (Figure 2Bvii) it is perhaps not surprising that we see no reaction. The extent to which lithium will progress into a ceramic electrolyte depends on a number of factors. If the cracks are wider and more numerous, then for the same quantity of charge passed, the Li front will not advance as far. To verify this, the volume of dendritic cracks within both multi-layered electrolytes after a plating capacity of 1 mAh cm^{-2} was calculated by Avizo. The crack volume for the case of Li_3ScCl_6 is 9.14 × 10^7 µm^3, which is more than twice the value of 4.15 × 10^7 µm^3 for $Li_{10}GeP_2S_{12}$, aligning with the fact that the Li front reaches the $Li_{10}GeP_2S_{12}$ layer but does not extend to the Li_3ScCl_6 layer for the same quantity of charge passed.

Li_3PS_4

XCT virtual cross-sections and 3D rendering of the cell with a Li_3PS_4 inner layer, i.e., Li/Li_6PS_5Cl/Li_3PS_4/Li_6PS_5Cl/Li, are presented in Figure 6. Spallations are again evident but in this case the transverse crack passes through the interface between Li_6PS_5Cl and the inner layer without deflection and continues largely unimpeded through the inner layer (Figures 6A and 6B). SEM images show the isotropic microstructure of the Li_3PS_4 (Figure S5). The cell is short circuited at 2.75 mA cm^{-2} (Figure 6C) comparable with Li_6PS_5Cl alone, (Figure S1) confirming that this inner layer provides no benefit in terms of dendrite crack mitigation, in contrast to Li_3ScCl_6 and $Li_{10}GeP_2S_{12}$.

The origins of crack deflection

Three mechanisms of inhibiting dendritic cracks have been observed when inner solid electrolyte layers are present, and without the need for high stack pressures as was suggested previously,[21] (1) crack deflection along the interface between layers; (2) within the inner layer before the arrival of lithium and (3) by lithium reaching the inner layer and reacting with it to block the cracks. The last of these, observed here for $Li_{10}GeP_2S_{12}$, is analogous to the process discussed previously.[21] The first two have not been reported before as far as we are aware. They are more general

Please cite this article in press as: Hu et al., Deflecting lithium dendritic cracks in multi-layered solid electrolytes, Joule (2024), https://doi.org/10.1016/j.joule.2024.06.024

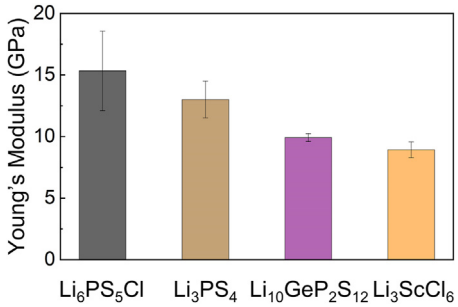

Figure 7. The Young's moduli of four types of solid electrolytes

The Young's moduli for Li_6PS_5Cl, Li_3PS_4, $Li_{10}GeP_2S_{12}$, and Li_3ScCl_6 are 15.3 (± 3.2) GPa, 13.0 (± 1.5) GPa, 9.9 (± 0.3) GPa, and 8.9 (± 0.6) GPa, respectively. Both $Li_{10}GeP_2S_{12}$ and Li_3ScCl_6 have relatively lower Young's moduli compared with Li_6PS_5Cl. Average values were obtained from three distinct regions within each sample, with 15–16 indents in each region. Error bars represent standard deviations.

mechanisms, especially deflection along the interface between layers. For each inner layer type, the same mechanism was consistently observed multiple times within the 3D tomographic images for each cell and across three repeat cells.

The observation of no deflection in the cell $Li/Li_6PS_5Cl/Li_3PS_4/Li_6PS_5Cl/Li$ indicates that crack deflection is not inherent in every multi-layered solid electrolyte. The fact that cracks deflect at the interface between Li_6PS_5Cl and Li_3ScCl_6 or $Li_{10}GeP_2S_{12}$ in the absence of lithium demonstrates that it is not essential to invoke reactivity with lithium metal to deflect cracks, instead this deflection has its origins in the mechanical properties of the interface. Growing cracks can be deflected by weak interfaces/boundaries in ceramics.[34] The Young's moduli of each of the inner layer electrolytes were measured by nanoindentation and the results are presented in Figure 7. There is a close match between the Young's moduli of Li_6PS_5Cl and Li_3PS_4, consistent with the dendritic crack passing across the interface unimpeded. The Young's moduli for Li_3ScCl_6 and $Li_{10}GeP_2S_{12}$ are both lower than Li_6PS_5Cl. While fabricating the layered electrolyte, different layers are joined by local bonding of particles. The surface tension (i.e., stress) between Li_6PS_5Cl and the inner layer solid electrolyte is influenced by pressing-induced residual stresses, exaggerated by dissimilarities in their moduli.[35] For bonding between two types of particles with dissimilar elastic moduli, tensile stress concentrations are expected to exist at their interfaces.[27,28] Higher tensile stress occurring perpendicular to the interface effectively weakens the interfacial bonding by reducing the applied stress required for the interface failure. In comparison with the bulk, the diminished bonding at the interface makes it susceptible to fracture when a crack approaches, thus altering the direction of crack propagation.

Let us now consider dendritic crack deflection within the solid electrolyte layer Li_3ScCl_6, which has a plate-like particle morphology. Similar mismatches in the elastic moduli (stiffness) between the dense and porous regions will again lead to weaknesses at the boundaries between the dense and porous regions, providing favorable pathways for the dendritic cracks around the dense particles. Due to the preferred orientation of the dense particles with their long axes parallel to the interface between the layers, the deflection is predominantly lateral.

Crack deflection is accompanied by the development of both normal and shear strains at the interfaces between Li_6PS_5Cl and Li_3ScCl_6 or $Li_{10}GeP_2S_{12}$. The strain

Please cite this article in press as: Hu et al., Deflecting lithium dendritic cracks in multi-layered solid electrolytes, Joule (2024), https://doi.org/10.1016/j.joule.2024.06.024

maps of the multi-layered electrolytes $Li_6PS_5Cl/Li_3ScCl_6/Li_6PS_5Cl$ and $Li_6PS_5Cl/Li_{10}GeP_2S_{12}/Li_6PS_5Cl$ were calculated using the gradients of the displacement field that is measured by DVC analysis from the XCT data. Maps of normal strains ε_{xx} and ε_{yy}, as well as shear strain γ_{xy}, of $Li_6PS_5Cl/Li_3ScCl_6/Li_6PS_5Cl$ and $Li_6PS_5Cl/Li_{10}GeP_2S_{12}/Li_6PS_5Cl$ are presented in Figures S6–S9, respectively. The tensile normal strains indicate crack opening. The evolutions of ε_{xx} and ε_{yy} closely correlate with the observed vertical crack propagation and lateral crack deflection. Particularly, the ε_{yy} maps show that the crack deflects along the Li_6PS_5Cl/Li_3ScCl_6 and $Li_6PS_5Cl/Li_{10}GeP_2S_{12}$ interfaces initially and then enters the inner layer; further deflecting laterally in the case of Li_3ScCl_6. Opening of the cracks within the inner Li_3ScCl_6 layer is also shown by the ε_{yy} maps. The shear strains indicate there are relative displacements parallel to the crack faces. This result verifies that crack deflection exhibits both crack opening and shearing, i.e., both loading modes I and II exist at the deflected cracks.[36]

It is known that the interface strength is influenced by the surface roughness, with increased roughness contributing to enhanced interfacial bonding and improved mechanical interlocking.[37] In this study, the surface roughness between Li_6PS_5Cl and the inner electrolytes is observed to be similar across the samples (Table S1). The interfacial mechanics are also known to be affected by interfacial reactions.[38,39] To consider this, powdered mixtures of Li_6PS_5Cl and, respectively, Li_3ScCl_6, $Li_{10}GeP_2S_{12}$, and Li_3PS_4 were prepared and examined by X-ray photoelectron spectroscopy (XPS) and ^{6}Li nuclear magnetic resonance (^{6}Li NMR) spectroscopy. Results are shown in Figure S10. There is no change in the P, S, Cl, and Ge signals between the individual Li_6PS_5Cl and $Li_{10}GeP_2S_{12}$ powders and the mixture, consistent with no reaction. Similarly, there are no changes in the XPS for the mixture of Li_6PS_5Cl and Li_3PS_4 (Figure S10). By contrast, the Li_6PS_5Cl and Li_3ScCl_6 mixture shows changes, in particular the disappearance of the phosphorus peak. ^{6}Li NMR confirms further reactivity of this mixture and indicates the formation of LiCl. Rosenbach et al. also observed the disappearance of the phosphorus signal and attributed it to the formation of Li_3P, which reacts with even trace amounts of H_2O forming volatile H_3P.[40] Therefore, we expect a reaction at the interface between Li_6PS_5Cl and Li_3ScCl_6. The impedances of discs composed of each of the four electrolytes and discs composed of the multi-layered electrolytes, $Li_6PS_5Cl/Li_3ScCl_6/Li_6PS_5Cl$, $Li_6PS_5Cl/Li_{10}GeP_2S_{12}/Li_6PS_5Cl$, and $Li_6PS_5Cl/Li_3PS_4/Li_6PS_5Cl$, all compacted at the same 400 MPa pressure were collected using blocking electrodes. The data were collected as a function of time. After initial equilibration the sum of the individual impedances closely matched those of the corresponding multi-layered electrolytes, indicating no significant impedances at the interfaces and no change with time (Figure S11).

The observation of crack deflection at the interface between Li_6PS_5Cl and Li_3ScCl_6 or $Li_{10}GeP_2S_{12}$ inner layers, with one inner layer exhibiting reactivity with Li_6PS_5Cl and the other not, suggests that the interfacial reaction is not the determining factor for introducing weak interfaces to deflect crack. Furthermore, Li_3PS_4 does not react with Li_6PS_5Cl and does not deflect dendrite cracks. It is the difference in the elastic moduli that fundamentally determines weak interfaces and dendrite deflection.

Conclusions

Three mechanisms of inhibiting lithium dendrites are considered when a solid electrolyte inner layer is included between two layers of the main solid electrolyte, two crack deflection mechanisms with a mechanical origin and the third, identified previously and involving reaction between lithium and the inner layer material. When the inner layers, Li_3ScCl_6 or $Li_{10}GeP_2S_{12}$, are present, lithium plating at current densities up to

Please cite this article in press as: Hu et al., Deflecting lithium dendritic cracks in multi-layered solid electrolytes, Joule (2024), https://doi.org/10.1016/j.joule.2024.06.024

at least 15 mA cm^{-2} is possible without a short-circuit compared with 2.75 mA cm^{-2} for the main Li_6PS_5Cl solid electrolyte on its own. Both inner layer materials deflect cracks along the interface with the Li_6PS_5Cl due to differences in the elastic moduli between them and Li_6PS_5Cl, leading to weakness at the interface providing favorable pathways for the deflected cracks. Li_3ScCl_6, which adopts a layered crystal structure, also deflects cracks laterally within the phase due to a high level of preferred orientation of the dense particles along the direction parallel to interface. Therefore, Li_3ScCl_6 introduces two crack deflection processes. The crack deflection at the interface between the two electrolytes and within the Li_3ScCl_6 occurs before Li reaches the inner layer, hence they have a mechanical rather than chemical origin. These findings inspire further development of fracture-tolerant solid electrolytes through (1) exploring other inner layer solid electrolytes exhibiting dissimilar elastic modulus from the main solid electrolyte, (2) modifying the electrolyte microstructure by introducing stiffer inclusions with preferred orientation, and (3) implementing other crack deflection mechanisms, for example, introducing residual stress in solid electrolytes.

EXPERIMENTAL PROCEDURES

Resource availability

Lead contact

Further information and requests for resources should be directed to and will be fulfilled by the lead contact, Peter G. Bruce (peter.bruce@materials.ox.ac.uk).

Materials availability

This study did not generate new unique materials.

Data and code availability

The data that support the findings of this study are available from the corresponding author upon reasonable request.

Synthesis of solid electrolytes

Li_3ScCl_6

LiCl and $ScCl_3$ (Sigma-Aldrich) were ground together in a 3:1 molar ratio using a mortar and pestle, and then sealed in a quartz tube under vacuum ($<10^{-5}$ mbar) before heating at 650°C for 12 h with a ramp/cooling rate of 2°C min^{-1}.

Li_3PS_4

Li_2S and P_2S_5 (Sigma-Aldrich) were mixed in a 3:1 molar ratio using a planetary ball mill, milled at 550 rpm for 7 h. The milled powders were pressed into discs under 400 MPa and heated at 400°C for 15 min with a ramp rate of 10°C min^{-1}. After heating, the discs were taken from the furnace and cooled within an Ar filled glovebox. The sintered discs were then ground into powders using a mortar and pestle.

Li_6PS_5Cl and $Li_{10}GeP_2S_{12}$ powders were purchased from MSE Supplies. PXRD patterns of the solid electrolyte powders are shown in Figure S12.

Symmetric cell assembly and cycling

To prepare multi-layered electrolytes, Li_6PS_5Cl powder was loaded into a stainless-steel die set followed by the addition of inner layer electrolyte powder (Li_3ScCl_6, $Li_{10}GeP_2S_{12}$, or Li_3PS_4). Subsequently, another portion of Li_6PS_5Cl powder was loaded into the die set and the three layers of powders were pressed into a 5 mm diameter disc under a uniaxial pressure of 400 MPa. The thicknesses of Li_6PS_5Cl/Li_3ScCl_6/Li_6PS_5Cl, Li_6PS_5Cl/$Li_{10}GeP_2S_{12}$/Li_6PS_5Cl, and Li_6PS_5Cl/Li_3PS_4/Li_6PS_5Cl are

Please cite this article in press as: Hu et al., Deflecting lithium dendritic cracks in multi-layered solid electrolytes, Joule (2024), https://doi.org/10.1016/j.joule.2024.06.024

999, 905, and 735 μm, respectively, as determined from the XCT. The porosities of all solid electrolyte discs were similar as determined by extracting the volume from XCT and the mass by weighing (Table S2). For monolithic Li_6PS_5Cl, Li_6PS_5Cl powders were pressed into a 5 mm disc under 400 MPa. 2 mm Li discs were attached onto both sides of the electrolyte discs. The assembly was then sealed into a pouch under vacuum (approximately 10^{-3} bar). All electrochemical tests were conducted using a Biologic VMP3 potentiostat, with the cells being maintained at room temperature and subjected to a stack pressure of 2.5 MPa.

XCT

X-ray tomograms of $Li/Li_6PS_5Cl/Li_3ScCl_6/Li_6PS_5Cl/Li$ and $Li/Li_6PS_5Cl/Li_{10}GeP_2S_{12}/Li_6PS_5Cl/Li$ cells were collected at the I13-2 beamline at Diamond Light Source. The imaging was run in pink beam mode with a peak energy of 22 keV. 2× objective was applied to obtain a pixel size of 1.625 μm. The exposure time was 0.023 s and the rotation angle was 180° per tomogram with a step of 0.045° (4,000 projections). X-ray tomograms of cells $Li/Li_6PS_5Cl/Li_3PS_4/Li_6PS_5Cl/Li$ and $Li/Li_6PS_5C/Li$ were collected by a Zeiss Xradia Versa 610 microscope at an accelerating voltage of 80 kV and a power of 10 W. For each tomogram, 3,201 projections were taken equiangularly over 360° with an exposure time of 2 s, leading to a pixel size of 1.625 μm.

SEM and PFIB-SEM

SEM images were collected using a Zeiss-Merlin microscope. PFIB sectioning was performed at 30 kV and 15 nA using a ThermoFisher Helios G4 Plasma-FIB instrument. SEM images were taken from the sectioned surfaces. For both SEM and PFIB-SEM, samples were transferred by an air-tight transfer holder to avoid exposure to air.

PXRD

The diffraction of the $Li_6PS_5Cl/Li_3ScCl_6/Li_6PS_5Cl$ electrolyte was collected at the I12 beamline (JEEP) at Diamond Light Source. Before acquiring diffraction data, X-ray radiography was used to locate the sample, ensuring that the X-ray beam passed through the center of the Li_3ScCl_6 inner layer. Subsequently, the imaging detector was replaced with a two-dimensional area diffraction detector. Transmitted diffraction was recorded using a monochromatic beam at 56 keV, reduced by slits to a spot size of 400 × 400 μm^2. Detector to sample distance was maintained as 1,200 mm. The diffraction data were analyzed using the Data Analysis WorkbeNch (DAWN) software.

XPS

Li_6PS_5Cl was mixed with Li_3ScCl_6, $Li_{10}GeP_2S_{12}$, and Li_3PS_4 in a weight ratio of 1:1, respectively, and pressed into discs under a uniaxial pressure of 400 MPa to obtain larger interfacial area for detecting the interfacial reactions between inner and outer layer electrolytes. XPS test was performed on these discs using a PHI Versaprobe III XPS under ultrahigh vacuum using an Al Kα monochromatic source, and was operated at a power of 25 W and an electron beam voltage of 15 kV. Samples were transferred into the instrument using an air-tight transfer module to prevent sample contamination. To ensure sampling of the bulk, data were acquired after sputtering a 1 × 1 mm^2 area with Ar^+ beam of 4 kV energy for 5 min. A pass energy of 55 eV was set to acquire core-level spectra. Data analysis was carried out using the CasaXPS software package. Spectra were fitted using a Shirley background and a Gaussian-Lorentzian lineshape. All spectra were charge referenced to adventitious carbon at 284.8 eV.

Please cite this article in press as: Hu et al., Deflecting lithium dendritic cracks in multi-layered solid electrolytes, Joule (2024), https://doi.org/10.1016/j.joule.2024.06.024

^{6}Li NMR

Li_6PS_5Cl and Li_3ScCl_6 were mixed in a weight ratio of 1:1, and pressed into a disc under 400 MPa. The disc was then ground and the resultant powder was used to detect the interfacial reactions by ^{6}Li NMR. Direct observation magic angle spinning (ν_R = 12 kHz) solid-state ^{6}Li (ν_0 = 58.89 MHz at 9.45 T) NMR was implemented to test the Li_6PS_5Cl/Li_3ScCl_6, LiCl, Li_6PS_5Cl, and Li_3ScCl_6 powders, using a 4 mm double air bearing probe. A 120-second relaxation time (>5T_1) was used and all spectra were referenced to the primary IUPAC (International Union of Pure and Applied Chemistry) standard (δ_{iso} = 0 ppm) of $LiCl_{(aq)}$.[41]

Mechanical testing

To measure the elastic modulus, nanoindentation tests were performed on Li_6PS_5Cl, Li_3PS_4, $Li_{10}GeP_2S_{12}$, and Li_3ScCl_6 discs. Each disc was mounted onto an SEM stub, as is standard practice for nanoindentation.[42] Employing the Hysitron PI 88 *in situ* nanoindenter, indents were conducted using a Berkovich tip under a high load regime, using single measurements. For the high load testing regime, three distinct regions within each sample were tested, with 15–16 indents in each region, at a range of loads from 10 to 400 mN. The storage modulus was calculated for each indent using the unloading curve, applying the method developed by Oliver and Pharr.[43] For the indents in each region, the mode of the modulus data was taken to produce a value of modulus vs. depth for each region. By taking the mean of all the data, the average expected value for the high load regime of each sample was calculated. The standard error of modulus was calculated from the variance and the number of tests conducted in one sample.

SUPPLEMENTAL INFORMATION

Supplemental information can be found online at https://doi.org/10.1016/j.joule.2024.06.024.

ACKNOWLEDGMENTS

P.G.B. is indebted to the Faraday Institution SOLBAT (FIRG007, FIRG008, FIRG026 and FIRG056), as well as the Engineering and Physical Sciences Research Council, the University of Oxford experimental equipment upgrade (EP/M02833X/1) and the Henry Royce Institute for Advanced Materials (EP/R0066X/1, EP/S019367/1, EP/R010145/1) for financial support. The authors thank Diamond Light Source for the provision of synchrotron radiation beam time. We acknowledge technical and experimental support at I13-2 beamline by S. Marathe and S. Kachkanov and at I12 beamline by O. Magdysyuk. We acknowledge use of characterization facilities within the David Cockayne Centre for Electron Microscopy, Department of Materials, University of Oxford.

AUTHOR CONTRIBUTIONS

B.H. contributed to all aspects of the research. B.H., S.Z., Z.N., X.G., S.D.P., and S.M. carried out the synchrotron XCT. B.H., Z.N., and L.W. processed the XCT data. B.H., S.Z., and X.G. prepared the electrolyte discs and cell assembly. B.H. and X.G. performed the SEM experiment. D.S.-J., L.Y., and B.H. conducted the XPS and PFIB experiment. J.P. and B.H. conducted the nanoindentation tests. G.J.R. performed the NMR. B.H. and G.B. carried out the synchrotron PXRD experiment. B.H., D.S.-J., D.L.R.M., S.Z., Z.N., X.G., T.J.M., and P.G.B. discussed the data. All authors contributed to the interpretation of data. B.H., D.S.-J., D.L.R.M., T.J.M., and P.G.B. wrote the manuscript with contributions and revisions from all authors. The project was supervised by T.J.M. and P.G.B.

DECLARATION OF INTERESTS

The authors declare no competing interests.

Received: January 8, 2024
Revised: February 27, 2024
Accepted: June 25, 2024
Published: July 19, 2024

REFERENCES

1. Janek, J., and Zeier, W.G. (2023). Challenges in speeding up solid-state battery development. Nat. Energy *8*, 230–240. https://doi.org/10.1038/s41560-023-01208-9.

2. Lee, Y.G., Fujiki, S., Jung, C., Suzuki, N., Yashiro, N., Omoda, R., Ko, D.S., Shiratsuchi, T., Sugimoto, T., Ryu, S., et al. (2020). High-energy long-cycling all-solid-state lithium metal batteries enabled by silver–carbon composite anodes. Nat. Energy *5*, 299–308. https://doi.org/10.1038/s41560-020-0575-z.

3. Yan, W., Mu, Z., Wang, Z., Huang, Y., Wu, D., Lu, P., Lu, J., Xu, J., Wu, Y., Ma, T., et al. (2023). Hard-carbon-stabilized Li–Si anodes for high-performance all-solid-state Li-ion batteries. Nat. Energy *8*, 800–813. https://doi.org/10.1038/s41560-023-01279-8.

4. Wan, H., Wang, Z., Liu, S., Zhang, B., He, X., Zhang, W., and Wang, C. (2023). Critical interphase overpotential as a lithium dendrite-suppression criterion for all-solid-state lithium battery design. Nat. Energy *8*, 473–481. https://doi.org/10.1038/s41560-023-01231-w.

5. Alexander, G.V., Shi, C., O'Neill, J., and Wachsman, E.D. (2023). Extreme lithium-metal cycling enabled by a mixed ion- and electron-conducting garnet three-dimensional architecture. Nat. Mater. *22*, 1136–1143. https://doi.org/10.1038/s41563-023-01627-9.

6. Janek, J., and Zeier, W.G. (2016). A solid future for battery development. Nat. Energy *1*, 16141. https://doi.org/10.1038/nenergy.2016.141.

7. Famprikis, T., Canepa, P., Dawson, J.A., Islam, M.S., and Masquelier, C. (2019). Fundamentals of inorganic solid-state electrolytes for batteries. Nat. Mater. *18*, 1278–1291. https://doi.org/10.1038/s41563-019-0431-3.

8. Kasemchainan, J., Zekoll, S., Spencer Jolly, D.S., Ning, Z., Hartley, G.O., Marrow, J., and Bruce, P.G. (2019). Critical stripping current leads to dendrite formation on plating in lithium anode solid electrolyte cells. Nat. Mater. *18*, 1105–1111. https://doi.org/10.1038/s41563-019-0438-9.

9. Liu, X., Garcia-Mendez, R., Lupini, A.R., Cheng, Y., Hood, Z.D., Han, F., Sharafi, A., Idrobo, J.C., Dudney, N.J., Wang, C., et al. (2021). Local electronic structure variation resulting in Li 'filament' formation within solid electrolytes. Nat. Mater. *20*, 1485–1490. https://doi.org/10.1038/s41563-021-01019-x.

10. Dixit, M.B., Vishugopi, B.S., Zaman, W., Kenesei, P., Park, J.S., Almer, J., Mukherjee, P.P., and Hatzell, K.B. (2022). Polymorphism of garnet solid electrolytes and its implications for grain-level chemo-mechanics. Nat. Mater. *21*, 1298–1305. https://doi.org/10.1038/s41563-022-01333-y.

11. Han, F., Westover, A.S., Yue, J., Fan, X., Wang, F., Chi, M., Leonard, D.N., Dudney, N.J., Wang, H., and Wang, C. (2019). High electronic conductivity as the origin of lithium dendrite formation within solid electrolytes. Nat. Energy *4*, 187–196. https://doi.org/10.1038/s41560-018-0312-z.

12. Lewis, J.A., Cortes, F.J.Q., Liu, Y., Miers, J.C., Verma, A., Vishnugopi, B.S., Tippens, J., Prakash, D., Marchese, T.S., Han, S.Y., et al. (2021). Linking void and interphase evolution to electrochemistry in solid-state batteries using operando X-ray tomography. Nat. Mater. *20*, 503–510. https://doi.org/10.1038/s41563-020-00903-2.

13. Doux, J.M., Nguyen, H., Tan, D.H.S., Banerjee, A., Wang, X., Wu, E.A., Jo, C., Yang, H., and Meng, Y.S. (2020). Stack pressure considerations for room-temperature all-solid-state lithium metal batteries. Adv. Energy Mater. *10*, 1903253. https://doi.org/10.1002/aenm.201903253.

14. Tu, Q., Shi, T., Chakravarthy, S., and Ceder, G. (2021). Understanding metal propagation in solid electrolytes due to mixed ionic-electronic conduction. Matter *4*, 3248–3268. https://doi.org/10.1016/j.matt.2021.08.004.

15. Sharafi, A., Kazyak, E., Davis, A.L., Yu, S., Thompson, T., Siegel, D.J., Dasgupta, N.P., and Sakamoto, J. (2017). Surface chemistry mechanism of ultra-low interfacial resistance in the solid-state electrolyte $Li_7La_3Zr_2O_{12}$. Chem. Mater. *29*, 7961–7968. https://doi.org/10.1021/acs.chemmater.7b03002.

16. Huo, H., Chen, Y., Zhao, N., Lin, X., Luo, J., Yang, X., Liu, Y., Guo, X., and Sun, X. (2019). In-situ formed Li_2CO_3-free garnet/Li interface by rapid acid treatment for dendrite-free solid-state batteries. Nano Energy *61*, 119–125. https://doi.org/10.1016/j.nanoen.2019.04.058.

17. Park, R.J.Y., Eschler, C.M., Fincher, C.D., Badel, A.F., Guan, P., Pharr, M., Sheldon, B.W., Carter, W.C., Viswanathan, V., and Chiang, Y.M. (2021). Semi-solid alkali metal electrodes enabling high critical current densities in solid electrolyte batteries. Nat. Energy *6*, 314–322. https://doi.org/10.1038/s41560-021-00786-w.

18. Han, X., Gong, Y., Fu, K.K., He, X., Hitz, G.T., Dai, J., Pearse, A., Liu, B., Wang, H., Rubloff, G., et al. (2017). Negating interfacial impedance in garnet-based solid-state Li metal batteries. Nat. Mater. *16*, 572–579. https://doi.org/10.1038/nmat4821.

19. Cheng, L., Chen, W., Kunz, M., Persson, K., Tamura, N., Chen, G., and Doeff, M. (2015). Effect of surface microstructure on electrochemical performance of garnet solid electrolytes. ACS Appl. Mater. Interfaces *7*, 2073–2081. https://doi.org/10.1021/am508111r.

20. Singh, D.K., Henss, A., Mogwitz, B., Gautam, A., Horn, J., Krauskopf, T., Burkhardt, S., Sann, J., Richter, F.H., and Janek, J. (2022). Li_6PS_5Cl microstructure and influence on dendrite growth in solid-state batteries with lithium metal anode. Cell Rep. Phys. Sci. *3*, 101043. https://doi.org/10.1016/j.xcrp.2022.101043.

21. Ye, L., and Li, X. (2021). A dynamic stability design strategy for lithium metal solid state batteries. Nature *593*, 218–222. https://doi.org/10.1038/s41586-021-03486-3.

22. Ning, Z., Jolly, D.S., Li, G., De Meyere, R., Pu, S.D., Chen, Y., Kasemchainan, J., Ihli, J., Gong, C., Liu, B., et al. (2021). Visualizing plating-induced cracking in lithium-anode solid-electrolyte cells. Nat. Mater. *20*, 1121–1129. https://doi.org/10.1038/s41563-021-00967-8.

23. Ning, Z., Li, G., Melvin, D.L.R., Chen, Y., Bu, J., Spencer-Jolly, D., Liu, J., Hu, B., Gao, X., Perera, J., et al. (2023). Dendrite initiation and propagation in lithium metal solid-state batteries. Nature *618*, 287–293. https://doi.org/10.1038/s41586-023-05970-4.

24. Wu, F., Fitzhugh, W., Ye, L., Ning, J., and Li, X. (2018). Advanced sulfide solid electrolyte by core-shell structural design. Nat. Commun. *9*, 4037. https://doi.org/10.1038/s41467-018-06123-2.

25. Miao, K., Hu, H., Dai, M., and Gao, C.-F. (2023). Rigid inclusion in an elastic matrix revisited. Arch. Appl. Mech. *93*, 1189–1199. https://doi.org/10.1007/s00419-022-02322-y.

26. Misseroni, D., Dal Corso, F., Shahzad, S., and Bigoni, D. (2014). Stress concentration near stiff inclusions: Validation of rigid inclusion model and boundary layers by means of photoelasticity. Eng. Fract. Mech. *121–122*, 87–97. https://doi.org/10.1016/j.engfracmech.2014.03.004.

27. Clegg, W.J., Kendall, K., Alford, N.M.N., Button, T.W., and Birchall, J.D. (1990). A simple way to make tough ceramics. Nature *347*, 455–457. https://doi.org/10.1038/347455a0.

28. Ming-Yuan, H., and Hutchinson, J.W. (1989). Crack deflection at an interface between dissimilar elastic materials. Int. J. Solids Struct.

25, 1053–1067. https://doi.org/10.1016/0020-7683(89)90021-8.

29. Yu, C., van Eijck, L., Ganapathy, S., and Wagemaker, M. (2016). Synthesis, structure and electrochemical performance of the argyrodite Li_6PS_5Cl solid electrolyte for Li-ion solid state batteries. Electrochim. Acta *215*, 93–99. https://doi.org/10.1016/j.electacta.2016.08.081.

30. Wenzel, S., Randau, S., Leichtweiß, T., Weber, D.A., Sann, J., Zeier, W.G., and Janek, J. (2016). Direct observation of the interfacial instability of the fast ionic conductor $Li_{10}GeP_2S_{12}$ at the lithium metal anode. Chem. Mater. *28*, 2400–2407. https://doi.org/10.1021/acs.chemmater.6b00610.

31. Bay, B.K., Smith, T.S., Fyhrie, D.P., and Saad, M. (1999). Digital volume correlation: Three-dimensional strain mapping using X-ray tomography. Exp. Mech. *39*, 217–226. https://doi.org/10.1007/BF02323555.

32. Liang, J., Li, X., Wang, S., Adair, K.R., Li, W., Zhao, Y., Wang, C., Hu, Y., Zhang, L., Zhao, S., et al. (2020). Site-occupation-tuned superionic Li_xScCl_{3+x} halide solid electrolytes for all-solid-state batteries. J. Am. Chem. Soc. *142*, 7012–7022. https://doi.org/10.1021/jacs.0c00134.

33. Zhou, L., Kwok, C.Y., Shyamsunder, A., Zhang, Q., Wu, X., and Nazar, L.F. (2020). A new halospinel superionic conductor for high-voltage all solid state lithium batteries. Energy Environ. Sci. *13*, 2056–2063. https://doi.org/10.1039/D0EE01017K.

34. Cook, J., and Gordon, J.E. (1964). A mechanism for the control of crack propagation in all-brittle systems. Proc. R. Soc. Lond. A *282*, 508–520. https://doi.org/10.1098/rspa.1964.0248.

35. Rana, A.K., Paul, S.K., and Dey, P.P. (2019). Stress field in an isotropic elastic solid containing a circular hard or soft inclusion under uniaxial tensile stress. Mater. Today Proc. *11*, 657–666. https://doi.org/10.1016/j.matpr.2019.03.024.

36. Hussain, M.A., Pu, S.L., and Underwood, J. (1973). Strain energy release rate for a crack under combined mode I and mode II. 1973 National Symposium on Fracture Mechanics, Part II *2*, 1–27. https://doi.org/10.1520/STP33130S.

37. Karehill, P.G., Glazer, M., and Nyström, C. (1990). Studies on direct compression of tablets. XXIII. The importance of surface roughness for the compactability of some directly compressible materials with different bonding and volume reduction properties. Int. J. Pharm. *64*, 35–43. https://doi.org/10.1016/0378-5173(90)90176-5.

38. Gladysz, G.M., Schmücker, M., Chawla, K.K., Schneider, H., Joslin, D.L., and Ferber, M.K. (1998). Characterization of the reaction products that develop in the processing of $Al_2O_3/BaZrO_3$ laminated composites. Mater. Charact. *40*, 209–214. https://doi.org/10.1016/S1044-5803(98)00011-4.

39. Tham, L.M., Gupta, M., and Cheng, L. (2001). Effect of limited matrix-reinforcement interfacial reaction on enhancing the mechanical properties of aluminium-silicon carbide composites. Acta Mater. *49*, 3243–3253. https://doi.org/10.1016/S1359-6454(01)00221-X.

40. Rosenbach, C., Walther, F., Ruhl, J., Hartmann, M., Hendriks, T.A., Ohno, S., Janek, J., and Zeier, W.G. (2023). Visualizing the chemical incompatibility of halide and sulfide-based electrolytes in solid-state batteries. Adv. Energy Mater. *13*, 2203673. https://doi.org/10.1002/aenm.202203673.

41. Harris, R.K., Becker, E.D., Cabral De Menezes, S.M., Goodfellow, R., and Granger, P. (2001). NMR nomenclature. Nuclear spin properties and conventions for chemical shifts (IUPAC recommendations 2001). Pure Appl. Chem. *73*, 1795–1818. https://doi.org/10.1351/pac200173111795.

42. Oliver, W.C., and Pharr, G.M. (1992). An improved technique for determining hardness and elastic modulus using load and displacement sensing indentation experiments. J. Mater. Res. *7*, 1564–1583. https://doi.org/10.1557/JMR.1992.1564.

43. Oliver, W.C., and Pharr, G.M. (2004). Measurement of hardness and elastic modulus by instrumented indentation: Advances in understanding and refinements to methodology. J. Mater. Res. *19*, 3–20. https://doi.org/10.1557/jmr.2004.19.1.3.